Nanoscale

PAPER

View Article Online
View Journal | View Issue

Cite this: *Nanoscale*, 2025, **17**, 20504

Probing defect formation in sulfur-annealed graphene for TMDC integration

Ahmad Nizamuddin Muhammad Mustafa, *[a,c] Victoria Greenacre, [d] Huanyu Zhou, [b] Shibin Thomas, [d] Tianyi Yin, [a] Sarah Alodan,[a] Yasir J. Noori, [e] Giuseppe Mallia, [b] Nicholas M. Harrison, [b] Gillian Reid, [d] Philip N. Bartlett, [d] Kees de Groot, [e] Sami Ramadan, *[a] Peter K. Petrov *[a] and Norbert Klein†[a]

The integration of graphene with other 2D materials has been extensively studied over the past decade to realize high-performance devices unattainable with single materials. Graphene-transition metal dichalcogenides (TMDCs) such as MoS_2, WS_2, $MoSe_2$, and WSe_2 vertical heterostructures have demonstrated promise in numerous electronic and optoelectronic applications due to the wide bandgap range and strong light–matter interaction in TMDCs, and the ability to form electrostatically tunable junctions with graphene. However, conventional methods for TMDCs growth, including chemical vapor deposition (CVD), electrodeposition, and atomic layer deposition (ALD), require high temperatures, which can degrade graphene's electrical and structural properties. Here, we investigate the impact of sulfur annealing on graphene, revealing significant etching and electrical degradation. Density functional theory (DFT) calculations identify the divacancy defect with two sulfur adatoms (DV-2S) and C–S–C bonds as the dominant defect, differing from the previously reported monovacancy with one sulfur adatom (MV-1S). This defect induces p-doping in graphene, consistent with experimental observations. To address these challenges, we introduce a protective strategy utilizing self-assembled monolayers (SAMs) during annealing, enabling the growth of high-quality WS_2 on graphene *via* electrodeposition. Our findings provide a foundation for integrating TMDCs with graphene while preserving its properties, advancing high-performance electronic and optoelectronic applications.

Received 10th May 2025,
Accepted 12th August 2025

DOI: 10.1039/d5nr01917f

rsc.li/nanoscale

1. Introduction

2D heterostructures composed of graphene and TMDCs have attracted intense research interest over the last decade due to their interesting physical properties and potential use in many novel device applications. These 2D materials exhibit unique properties compared to those of their 3D counterparts, and their flexibility leads to the ability to create new functionalities that cannot be achieved with single materials. Graphene is an attractive material for use in biosensors[1,2] and high-speed electronic[3] and optoelectronic devices[4] due to its remarkable mobility, broad bandwidth, and biocompatibility.[5] TMDCs such as MoS_2, WS_2, $MoSe_2$, and WSe_2 have been chosen for many electronic and optoelectronic applications due to their band gap range and strong exciton confinement.[6,7] The absence of dangling bonds in graphene and TMDCs allows their integration into heterostructures, enabling new devices that can outperform counterparts composed of single materials.[8]

By combining graphene with TMDCs, various device concepts have been demonstrated, such as novel transistors, memory devices, photodetectors, plasmonic, and solar cells.[9–11] Most such devices and functionalities have been fabricated by stacking individual layers of different materials using mechanical exfoliation method, which limits their large-scale application.[12] Recently, CVD, electrodeposition, and ALD have been developed to grow TMDC materials on graphene directly. These methods can offer large-area growth for mass production and allow the study of new device physics and applications. However, exposure to high temperatures during material growth or post-growth is required in such methods in

[a]*Department of Materials, Imperial College London, London SW7 2AZ, UK. E-mail: a.bin-muhammad-mustafa21@imperial.ac.uk, s.ramadan@imperial.ac.uk, p.petrov@imperial.ac.uk*
[b]*Department of Chemistry and Institute for Molecular Science and Engineering, Imperial College London, London W12 0BZ, UK*
[c]*Universiti Teknikal Malaysia Melaka, Hang Tuah Jaya, 76100 Durian Tunggal, Melaka, Malaysia*
[d]*School of Chemistry, University of Southampton, Southampton SO17 1BJ, UK*
[e]*School of Electronics and Computer Science, University of Southampton, Southampton, SO17 1BJ, UK*
† Norbert Klein passed away shortly after the completion of this work.

order to deposit crystalline TMDCs. Usually, the growth of MoS_2 or WS_2 involves the use of sulfur precursors in powder, liquid, or gas phases. However, sulfur has been found to interact with graphene at high temperatures and to change its properties.[13] The annealing of graphene at high temperatures under different conditions has already been reported to induce changes in its structure and electrical properties.[14] We have recently demonstrated that the degradation of the electrical properties of graphene can be ameliorated by coating graphene with a self-assembly monolayer under high temperatures in oxygen conditions.[15]

In this work, we systematically study the impact of annealing in the presence of sulfur on graphene's electrical and structural properties for use in applications that involve the growth of TMDCs on graphene. Samples were annealed at different temperatures from 300 °C to 800 °C under various conditions. DFT simulation was performed with range-separated hybrid exchange–correlation functionals in order to identify the role of sulfur in the doping and electronic properties of graphene. Furthermore, graphene device structures were fabricated to study the effect of the annealing conditions on device performance. We implemented strategies to improve the quality of graphene during the growth of TMDCs. To demonstrate this strategy, we electrodeposited WS_2 on graphene and studied the effect of post-processing sulfur annealing conditions on its properties.

2. Experimental

2.1. Materials and methods

Monolayer CVD-grown graphene on copper foil was purchased from Graphenea and SiO_2/Si substrates (wafers) were purchased from Graphene Supermarket. Graphene on SiO_2/Si samples were prepared by transferring CVD-grown graphene on SiO_2/Si substrates. To protect the graphene and reduce cracks during the transfer process, a layer of polymethyl methacrylate (PMMA) was spin-coated on top of the graphene/copper foil stack at 7700 RPM to act as a buffer layer. Subsequently, the PMMA/graphene/copper film stack was floated on a solution of ammonium persulfate (APS) (0.07 g mL^{-1} in H_2O) for 12 hours to remove the copper layer. The PMMA/graphene stack was then rinsed by floating it on two consecutive ultra-pure DI water baths for up to 1 hour per bath. The PMMA/graphene film was transferred onto the SiO_2/Si substrate by carefully scooping it from under the water. Next, the PMMA/graphene/substrate stack was baked on a hotplate for 1.5 hours at 180 °C to enhance the adhesion of graphene to the substrate. Finally, the PMMA/graphene/substrate was submerged in acetone overnight to remove the PMMA layer. The sample was subsequently annealed at 250 °C for 5 hours to eliminate any remaining PMMA residue on the graphene surface.

In addition, the sample corresponds to the hexamethyldisilazane (HMDS) coating with configuration HMDS/graphene on SiO_2/Si structure, where the HMDS treatment was applied after the graphene transfer process. The HMDS coating treatment involved immersing the substrate in an HMDS solution at room temperature for 12 hours so as to form a uniform self-assembled monolayer on the substrate surface (see SI).

Annealing method. After the sample preparation process, all graphene on SiO_2/Si samples were subjected to a subsequent annealing process. Annealing was performed using a Lenton Tube furnace in a quartz glass tube containing ~20 mg of sulfur placed at one end, adjacent to the sample, in a sealed system under a static vacuum (~1×10^{-2} mbar). The quartz tube was cycled between vacuum and N_2 (to remove air/oxygen) on standard Schlenk line apparatus before being left under static vacuum and inserted into the furnace. Each sample was purged with N_2 gas before being sealed under vacuum with the elemental sulfur. The samples were annealed in this sulfur environment for 10 minutes at temperatures of 300 °C, 400 °C, or 500 °C. Some of the samples were further annealed at 800 °C in a vacuum for 15 minutes. Similarly, samples of graphene with HMDS coating were annealed under the same condition; annealed in the sulfur environment for 10 minutes at a temperature of 400 °C, followed by annealing at 800 °C in a vacuum for 15 minutes. After annealing all sulfur condensed to the other side of the tube furnace where it was cooler, leaving no residue at the original sulfur location.

Electrodeposition of WS_2 on Gr. A WS_2 film was grown on HMDS-coated graphene using the electrodeposition method, with $[NEt_4]_2[WS_2Cl_4]$ as the precursor. The electrolyte solution consisted of 5 mM $[NEt_4]_2[WS_2Cl_4]$ and 0.1 M $[N^nBu_4]Cl$ as the supporting electrolyte. Electrodeposition was performed in a three-electrode system using an Autolab potentiostat (μAUT70706). A platinum disc (1 cm diameter) served as the counter electrode, while an Ag/AgCl electrode (0.1 M $[N^nBu_4]Cl$ in CH_2Cl_2) was used as the reference electrode. Detailed electrochemical characterization of $[NEt_4]_2[WS_2Cl_4]$ is available in our previous work.[16,17] WS_2 was deposited potentiostatically at −1.7 V *vs.* Ag/AgCl for 5 minutes. After the electrodeposition, the substrates were rinsed with fresh CH_2Cl_2 solvent followed by isopropyl alcohol and dried. Following deposition, the WS_2 films were annealed at 400 °C in N_2 gas with sulfur under reduced pressure (~1×10^{-2} mbar) for 1 hour to induce crystallization. The sample was annealed following the same procedure as the graphene samples with HMDS coatings.

2.2. Characterization

Surface defects were analyzed using optical images captured with an Olympus System BX51 compound optical microscope equipped with a 100× objective lens. Atomic force microscopy (AFM) images were acquired using an Asylum MFP-3D instrument in tapping mode, equipped with SCOUT 70 tips.

Raman characterization was performed using the HORIBA LabRAM HR Evolution Raman spectrometer. Raman spectroscopy was conducted using a laser with a wavelength of 532 nm (corresponding to an excitation energy EL = $\hbar wL$ = 2.33 eV). The set-up included an optical fibre and a 100× objective lens with a numerical aperture (NA) of 0.8, resulting in a laser spot size of 0.4 μm. An ND filter was used in order to maintain

the laser power below 2 mW. The Raman peak positions were calibrated with reference to the silicon peak at 520.7 cm^{-1}.

XPS characterization was conducted using a Thermo Fisher K-Alpha+ spectrometer. The XPS measurements employed an Al radiation source operating at the Kα+ line ($h\nu$ = 1486.6 eV). To ensure accurate spectroscopic analysis, the measurements were performed in an ultrahigh vacuum chamber with a base pressure of 5×10^{-8} bar.

Electrical measurements. Graphene was patterned using optical lithography, and 10/60 nm Cr/Au was then deposited onto the samples using a thermal evaporator. Finally, the lift-off process was performed using acetone to remove the photoresist. Two-probe measurements were used to measure the electrical characteristic (resistance) at room temperature using a B1500A Semiconductor Analyzer.

2.3. DFT simulation

The DFT calculations reported here are based on CRYSTAL23.[18–20] The range-separated hybrid exchange–correlation functional HSE06[21] was adopted to reduce self-interaction error, the non-negligible influence of which on the electronic structures of graphene-based systems has been widely reported in the literature.[22–26] A 6-21G* basis set modified for condensed matter calculations was used for carbon (C),[27] while Pople's 6-31G* basis set was used for sulfur (S).[28] All-electron DFT was performed in order to study the binding energy of the S 2p orbital. Models with 2-dimensional (2D) periodicity were generated for doped graphene, with the non-periodic direction aligned to the z axis. A 24 × 24 Monkhorst–Pack mesh was generated to sample the first Brillouin zone (1BZ) of the graphene primitive cell, which achieves an accuracy $<10^{-5}$ Hartree per atom. Considering the semi-metallic nature of graphene, the finite temperature Mermin smearing of 10^{-4} Hartree was used. The convergence criterion of total energy is 10^{-8} Hartree. All the structures are fully relaxed with the BFGS algorithm. The convergence criteria are 3×10^{-4} Hartree per Bohr for the energy gradient and 1.2×10^{-3} Bohr for displacement. The optimized lattice constant of graphene is 2.45 Å, which agrees well with the value obtained by X-ray diffraction (2.46 Å).[29] For comparison with experimental data, carrier concentrations at Fermi level and 300 K were computed with the BOLTZTRA keyword.[20]

A series of 2D supercells, including 4 × 4, 5 × 5, 8 × 8 and 10 × 10, was used to simulate various defect densities which correspond to samples annealed with S at different temperatures. A 6 × 6 *k*-point mesh was used for 4 × 4 and 5 × 5 supercells, while a 3 × 3 *k*-point mesh was used for 8 × 8 and 10 × 10 supercells. The chosen *k*-point meshes explicitly sample the Dirac cone, which is folded to the K point of supercell 1BZs in all cases. The defect formation energy of the substitution mechanism, E_f^{sub}, is the energy needed to substitute a C atom with a S atom from the pristine graphene lattice:

$$E_f^{sub} = \frac{1}{n}[(E_{SG} + n\mu_C) - (E_G + n\mu_S)] \quad (1)$$

E_{SG} (E_G) is the total energy of S-doped (pristine) graphene, μ_C (μ_S) is the chemical potential of a single C (S) atom in graphene (S_8 molecule), and n is the number of S atoms in the simulation cell. The formation energy of incorporation mechanism, E_f^{inc}, is the energy needed to incorporate an S atom into an existing vacancy:

$$E_f^{inc} = \frac{1}{n}[E_{SG} - (E_{VG} + n\mu_S)] \quad (2)$$

where E_{VG} is the total energy of graphene with vacancy defects.

3. Results and discussion

3.1. Impact of sulfur annealing on graphene's structural integrity

Two sets of samples were annealed under different conditions. The first set was annealed in the presence of sulfur at temperatures of 300 °C, 400 °C, and 500 °C, and the second set was annealed at 300 °C, 400 °C, and 500 °C with sulfur and then at 800 °C in vacuum. We employed high temperature annealing because the crystallinity of the TMDCs can be improved at elevated temperatures.[30] Additionally, the majority of TMDCs grown *via* CVD are synthesized at temperatures above 700 °C.[31–33] Another graphene sample was annealed at 800 °C in vacuum to be used as a reference sample. Fig. 1 shows the evolution of the graphene sample under different annealing conditions, while Fig. S1(a) shows a typical graphene surface before annealing with islands of multilayer graphene (dark purple spots) resulting from the CVD graphene growth process.[34] However, in the sample which underwent 800 °C vacuum annealing, the graphene starts to display defects, with the presence of etched pit spots, as shown in Fig. 1(a). Samples annealed at 300 °C, 400 °C, and 500 °C under sulfur conditions (Fig. S1(b)–(d)) show no visible indications of etched pits spots. However, samples that underwent annealing with sulfur followed by annealing at 800 °C in vacuum (Fig. 1(b)–(d)) exhibit noticeable faded spots indicating etched pits on the graphene surface with some spots are circled with red dash. The presence of the etched pits becomes more pronounced with increasing annealing temperature in the presence of sulfur. To estimate the etched area, 6 images (140 μm × 105 μm) at 100× magnification were taken for each sample and were processed in black and white. Analysis revealed that the sample annealed at 800 °C in vacuum had an etched area of 2.3% of the total area. Meanwhile, annealing at 300 °C with sulfur followed by at 800 °C in vacuum resulted in an etched area of 7.3%, whereas the corresponding annealing at 400 °C resulted in an etched area of 8.5%, and that at 500 °C resulted in an etched area of 11.0% (Fig. S2). To conduct a more detailed assessment of the presence of etched pits on the graphene surface, samples were characterized using AFM and the results are shown in Fig. 1(e)–(h). The dark spots in AFM images correspond to etched pits. Colored lines were drawn on each AFM image to extract the line profiles of the etched pits, as shown in Fig. 1(i). The etch profiles revealed that the pit

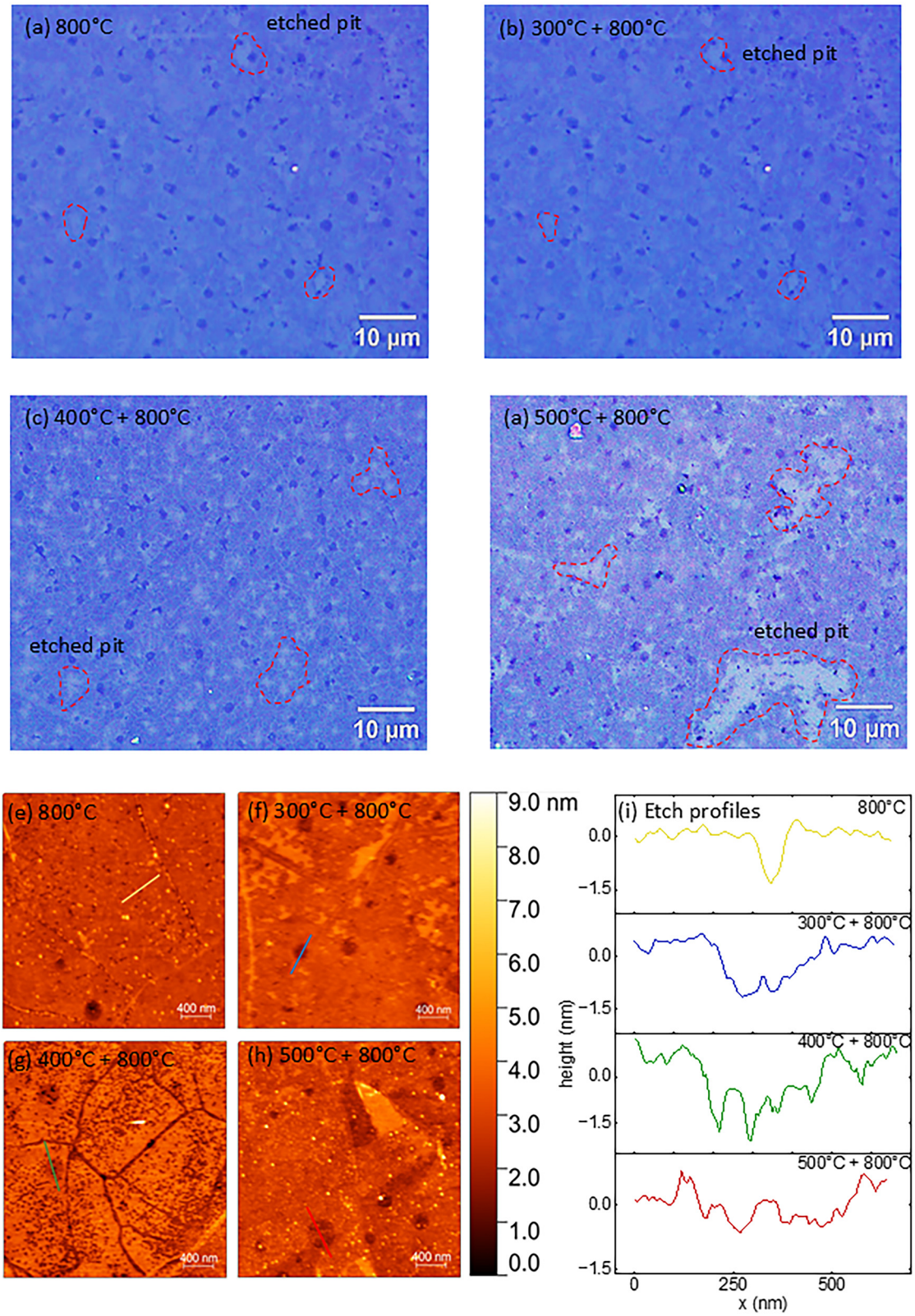

Fig. 1 Graphene surface defects under various annealing conditions. (a) Graphene exhibits initial defects with the emergence of etched pit spots after 800 °C vacuum annealing. Samples annealed at (b) 300 °C, (c) 400 °C, and (d) 500 °C with sulfur followed by 800 °C vacuum annealing exhibit prominent etched pits, the prevalence of which intensifies with increasing annealing temperature. (e)–(h) AFM images of graphene annealed at: (e) 800 °C vacuum, (f) 300 °C in sulfur + 800 °C vacuum, (g) 400 °C in sulfur + 800 °C vacuum, (h) 500 °C in sulfur + 800 °C vacuum, with the dark spots in AFM images correspond to etched pits. The AFM analysis validates the presence of etched pits (line profile of etched pits) on the graphene surface resulting from sulfur annealing, and (i) etch pits profile measured with AFM.

depths varied, reaching up to approximately 2 nm, with widths ranging from 50 nm to 500 nm. This analysis confirmed the presence of etch pits in the graphene resulting from sulfur annealing.

To gain further insight into the presence of sulfur, an X-ray photoelectron spectroscopy (XPS) analysis was conducted specifically focusing on the sulfur 2p (S 2p) region. The results shown in Fig. 2 confirm the presence of sulfur in the samples annealed at 300 °C, 400 °C, and 500 °C. This is evident from the appearance of the S 2p peak at 163.3 eV, 163.1 eV, and 164.1 eV for samples annealed in the presence of sulfur at 300 °C, 400 °C, and 500 °C respectively. This peak corresponds to the C–S–C bond.[35] Another prominent peak at approximately 164.3 eV, 164.4 eV, and 165.5 eV for samples annealed at 300 °C, 400 °C, and 500 °C respectively indicates a splitting of the C–S–C bond peak, which is probably due to the relativistic effects of S 2p. These peaks suggest the formation of a covalent bond between sulfur and carbon. However, in samples annealed at 300 °C, 400 °C, and 500 °C with sulfur followed by 800 °C in vacuum, the intensity of peaks corresponding to the C–S–C bond is relatively small. As shown in Fig. 2(b), the intensity increases with the rise in annealing temperature with sulfur, where values of its atomic concentration relative to carbon are estimated to be 2.03%, 3.53%, and 4.18% for samples annealed at 300 °C, 400 °C, and 500 °C with sulfur respectively. Further annealing at 600 °C and 700 °C with sulfur leads to an increase in sulfur according to the XPS analysis, as shown in Fig. S3(a)–(b). However, the S 2p peaks nearly vanish in all samples that subsequently undergo annealing at 800 °C in vacuum, with atomic concentrations in all cases of less than 1.1%. This indicates that the annealing process involving sulfur potentially triggers the formation of covalent bonds with carbon. Consequently, the subsequent annealing at 800 °C in vacuum leads to the evaporation of sulfur, which correlates with the observed increase in etched pits on the graphene layer.

The potential role of residual oxygen in defect formation during thermal treatments is indeed important to consider, particularly under high-temperature conditions. To address this concern, we included a comparative analysis based on our prior study,[15] in which graphene was exposed to oxygen-rich environments at high temperatures. In that work, while electrical degradation (*e.g.*, p-doping and increased resistance) was observed due to oxygen adsorption and weak covalent bonding, no significant etching or pit formation was observed. These findings indicate that oxidative processes alone do not account for the extensive structural damage (etch pits) observed in our sulfur-annealed samples.

Moreover, we analyzed the O 1s region for samples annealed under sulfur at 300 °C, 400 °C, and 500 °C (Fig. S4(b)–(d)). All sulfur-annealed samples exhibit a relatively sharp O 1s peak centered between 531.8 eV and 532.7 eV, representing a slight shift from the ~532.6 eV signal observed in pristine graphene (Fig. S4(a)). This shift may originate from S–O bonding or oxidation of sulfur residues. In contrast, typical reduced graphene oxide, formed under oxidative conditions, exhibits a broad and multi-component O 1s peak due to various oxygen-containing functional groups such as hydroxyl (C–OH), carbonyl (C═O), epoxy (C–O–C), and carboxyl (O═C–O),[36–38] which are not noticeable in our samples. This suggests minimal direct oxidation of graphene during sulfur annealing. Thus, these results support our conclusion that the enhanced etching observed after post-annealing at 800 °C is driven by the desorption and rearrangement of sulfur-induced defects, such as C–S–C bonds, rather than oxidative etching. The degree of etching correlates with the initial sulfur content (as confirmed by XPS S 2p data), further reinforcing the sulfur-specific nature of the defect mechanism.

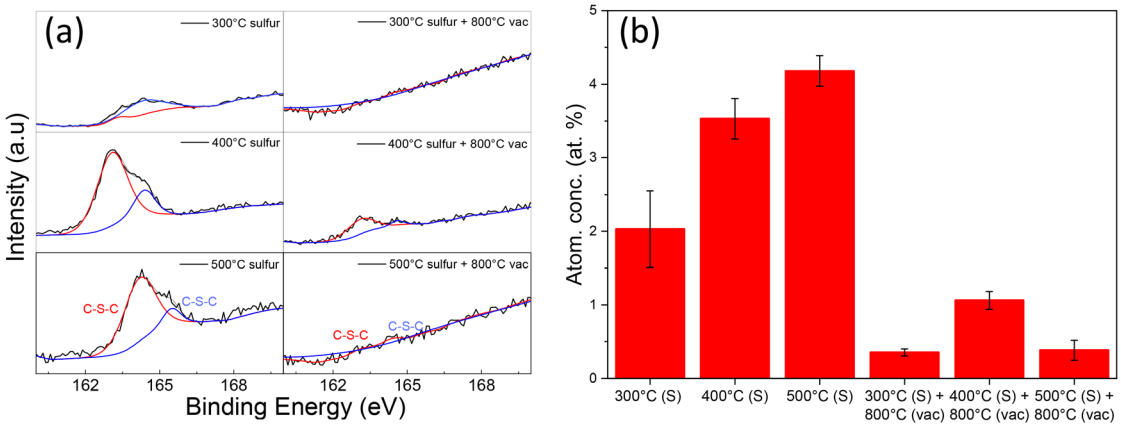

Fig. 2 Presence and bond formation of sulfur characterized by XPS. (a) High-resolution XPS spectra of the sulfur 2p (S 2p) region confirms its presence in samples annealed at different temperatures under sulfur conditions. Peaks corresponding to C–S–C bonds show splitting and are observed at approximately ~163 eV and ~165 eV. (b) Quantification of the S 2p peak intensities reveals increases at higher annealing temperatures with sulfur, where atomic concentrations relative to carbon are estimated at 2.03%, 3.53%, and 4.18% for samples annealed at 300 °C, 400 °C, and 500 °C respectively. Conversely, samples annealed at 800 °C in vacuum exhibit a significant reduction in S 2p peaks.

3.2. Strain and doping effects on graphene

The Raman spectrum was analyzed, and the results are presented in Fig. 3. In addition to the typical D, G, and 2D peaks (ω_D, ω_G and ω_{2D} respectively), other notable peaks (Fig. S5) at 1265 cm^{-1}, 1432 cm^{-1} and 1558 cm^{-1} respectively are observed in samples annealed at 300 °C, 400 °C, and 500 °C under sulfur conditions. These peaks are indicative of carbon–sulfur bonding, as also observed by Odunmbaku *et al.*,[39] and the peak at 1558 cm^{-1} is believed to originate from C–S vibration due to the out-of-plane or antisymmetric stretching vibrations v3 of CS_2.[35] The intensities of these peaks increase with higher annealing temperatures under sulfur conditions, but almost vanish in samples that undergo further annealing at 800 °C in vacuum, as shown in Fig. 3(b). This is in accordance with the XPS results shown in Fig. 2(a) which reveal the evaporation of sulfur.

To investigate spatial variations in defect density, the intensity ratio of the D and G bands (I_D/I_G) was mapped across the graphene surface (Fig. S6). While the spatial resolution of the Raman mapping is limited by the laser spot size (~3 μm), the maps qualitatively illustrate the distribution of defects. Analysis of I_D/I_G across the mapped regions (Fig. S6(d)) reveals a clear trend: defect density increases with an annealing temperature. This supports our conclusion that sulfur-induced defects become more prevalent as the annealing temperature rises.

Furthermore, the Raman spectra analysis of the samples indicates notable upshifts in ω_G and ω_{2D} compared to those of the intrinsic graphene which are typically observed at around 1583 cm^{-1} (ω_G^0) and 2678 cm^{-1} (ω_{2D}^0) respectively.[40] The ω_G peak appearing at 1596 cm^{-1} for sample annealed at 300 °C in sulfur. This peak gradually upshifts to 1600 cm^{-1} for the sample annealed at 500 °C in sulfur followed by 800 °C in vacuum. Similarly, the ω_{2D} peak appears at 2689 cm^{-1} for the sample annealed at 300 °C in sulfur. Then gradually upshift to 2701 cm^{-1} for sample annealed at 500 °C in sulfur followed by

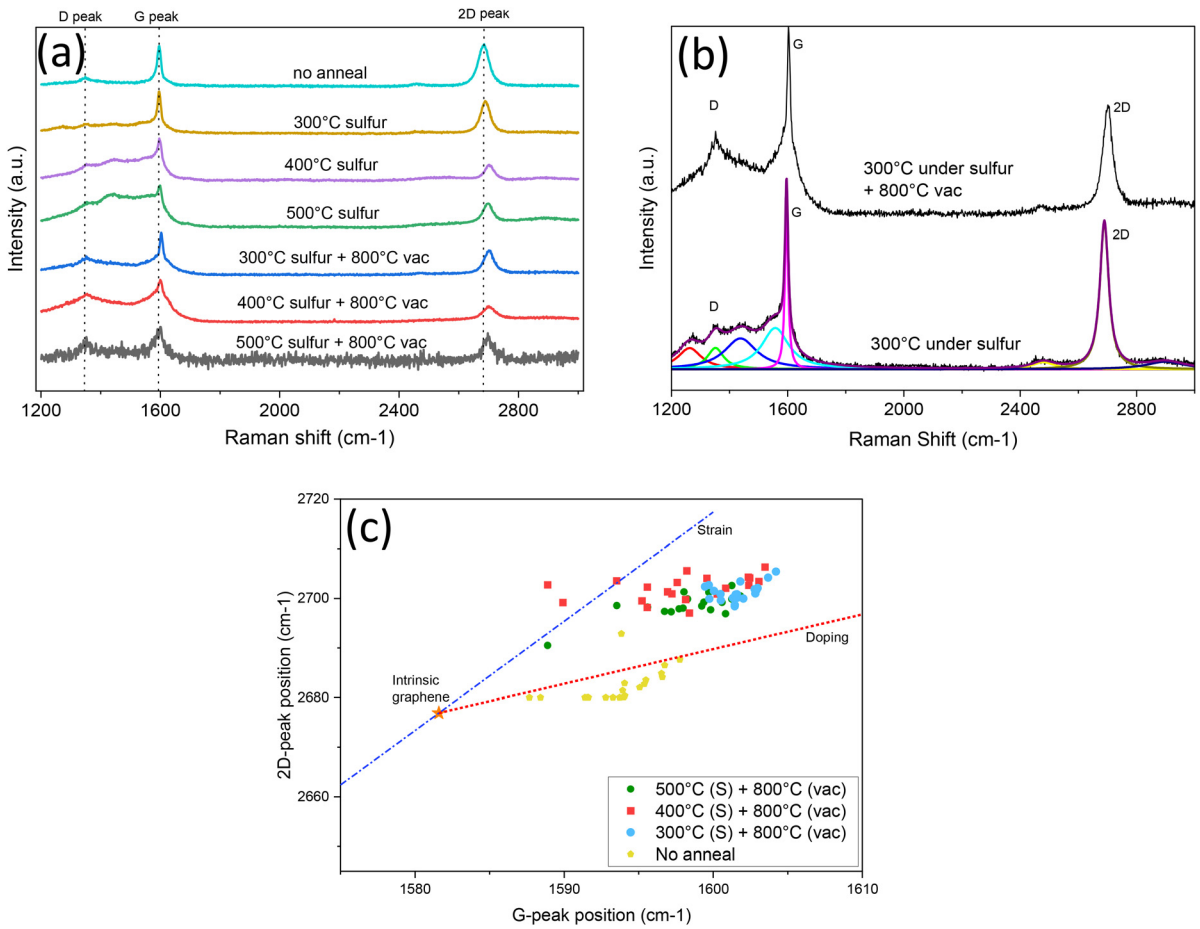

Fig. 3 Raman spectroscopy analysis of graphene samples annealed under various conditions. (a) Raman spectra depicting the D, G, and 2D peaks (ω_D, ω_G and ω_{2D}) in addition to distinct peaks at 1432 cm^{-1} and 1558 cm^{-1} observed in samples annealed at 300 °C, 400 °C, and 500 °C under sulfur conditions and at those temperatures with subsequent 800 °C in vacuum, where the intensities of the peaks show a temperature-dependent increase. (b) Comparison of samples annealed at 300 °C with sulfur and those at 300 °C with sulfur + 800 °C vacuum, showing that in the latter the convoluted peaks almost disappear which is consistent with the XPS results indicating the evaporation of the sulfur. (c) Analysis of correlation of 2D–G peak positions (ω_G and ω_{2D}) against the associated strain and doping levels, with reference lines adapted from Lee *et al.*[41] Data points below the red dashed line indicate doped but strain-free graphene, while those above the blue dashed line indicate strained but doping-free graphene.

800 °C in vacuum. These shifts could be attributed to either doping or strain or a combination of both.[41]

The correlation between the 2D–G peak positions (ω_G and ω_{2D}) and strain/doping is depicted in Fig. 3(c), and the plot includes reference lines for strain and doping as previously reported by Lee *et al.*[41] Lee and co-workers proposed a method to quantify strain (ε) and doping (n) in graphene using Raman spectra in a correlation analysis of ω_G and ω_{2D} to determine ε and n separately based on prior assumptions and experimental data. Both experimental[42–46] and theoretical[47–50] studies have shown that, for single-layer graphene (SLG) with constant ε and varying n or *vice versa*, the positions of the G and 2D peaks in the ω_G and ω_{2D} vector form a straight line (represented by the blue dashed line for pure strained graphene and the red dashed line for pure doped graphene). Thus, data points falling below the red dashed line indicate doped but strain-free graphene, whereas data points above the blue dashed line indicate strained but doping-free graphene. Data points falling under the strain line and above the red line indicate both strained and doped graphene. The intrinsic graphene which is free from doping and strain is represented by peaks at around 1583 cm^{-1} (ω_G^0) and 2678 cm^{-1} (ω_{2D}^0) at the meeting point of the blue dashed and red dashed lines. The analysis of our samples reveals that increasing the annealing temperature under sulfur conditions leads to a greater impact of doping and strain on the graphene, while further annealing at 600 °C and 700 °C in the presence of sulfur leads to the strain and doping becoming saturated (Fig. S7). The strain observed in graphene can be attributed to the differences in thermal expansion coefficients between graphene and the underlying substrate. Previous studies such as that by Ryu *et al.*[51] have reported that the annealing of graphene on SiO_2 substrates at 300 °C results in significant structural deformation, causing the formation of sub-nanometer-high ripples with a lateral quasi-period of several nanometers. These observations suggest that strain arises from the corrugation or rippling of the graphene sheet.[52]

Strain and doping in graphene samples can be quantified by deriving values from the peak shift in the Raman (ω_G and ω_{2D})[42,53] using established equations provided in SI. Initially, the carrier concentration indicates p-type doping with $n \sim 4.0 \times 10^{11}$ cm^{-2}, which increases significantly after annealing at 300 °C, 400 °C, and 500 °C with sulfur to reach $n \sim 1.3 \times 10^{12}$ cm^{-2}. Further annealing at 800 °C in vacuum after sulfur treatment enhances the doping effect, whereas samples annealed only at 800 °C exhibit lower carrier concentrations. Strain values also increase with sulfur annealing, showing compressive strain of up to +0.58% which remained high even after subsequent vacuum annealing at 800 °C. The results suggest that sulfur enhances both doping and strain effects during the annealing process. We then prepared new samples and annealed them at 300 °C, 400 °C, and 500 °C in vacuum for comparison with the sulfur-annealed samples. The results of Raman analysis (Fig. S8) show that the samples annealed without sulfur were only slightly strained compared with those annealed in the presence of sulfur. This further supports the conclusion that the strain was originally induced by sulfur annealing.

3.3. Defect (sulfur-doping) formation in graphene by DFT calculation

Considering the experimentally characterized C–S–C bond, the DV-2S defect, featuring two C–S–C bonds, is modelled at various densities (as detailed in the section 2), where 2 neighboring C atoms in the same primitive cell are substituted by 2 S atoms. Previous DFT studies also reported a MV-1S defect,[54,55] where a C atom is substituted by a non-conventional tricoordinate S atom. Fig. 4(a) and (b) illustrates the fully relaxed structures of DV-2S and MV-1S in the 5 × 5 supercell. In DV-2S, the higher S concentration induces more significant repulsion and local strain, pushing S atoms above the plane and generating out-of-plane ripples across the sheet. Interestingly, as defect density decreases, the height of S atoms increases while the area of the induced out-of-plane ripple decreases, which probably indicates the increasingly localized influence of DV-2S. In comparison, the tricoordinate S of MV-1S is closer to the graphene plane due to lower repulsion. The height of the S atom also increases as defect density decreases, following a similar trend to that in DV-2S. The ripple in MV-1S is almost negligible and is limited to the 3 nearest neighbors of S.

XPS spectra reveals the correlation between doping and the shift in the S 2p peak. In order to identify the preferred structure in S-doped graphene, the binding energy of S 2p orbital is computed based on Koopmans' theorem, which approximates the binding energy BE by BE = $-E$, where E is the ionization energy.[56] Fig. 4(c) and (d) illustrates the shift at various carrier densities. In both DV-2S and MV-1S, the majority charge carriers are holes as in the synthesized S-doped graphene. The measured carrier density (~8.3×10^{11} to ~1.3×10^{12} cm^{-2}) also lies in the simulated ranges for both defects. The binding energies of DV-2S follow a similar pattern but with a difference of ~3 eV, which might be due to the approximation used. It should also be noted that DV-2S is a relatively simple model of a C–S–C bond. Other probable S-doped defects can be experimentally characterized,[57] which is beyond the scope of this work. MV-1S has been reported as an n-doped metal by Tuček *et al.*,[55] while in this study it is characterized as a p-doped semiconductor. That is probably due to the lower concentrations of S used here, as the metallic transition is reported by Denis *et al.*[54] around 4 at%. Although the computed binding energy of MV-1S shows better agreement with the XPS data, its evolution with carrier density exhibits an opposite trend, suggesting a distinctly different chemical environment.

To further probe these defect structures, the Becke electron localization functions (ELF) up to the third nearest neighbors were calculated for both DV-2S and MV-1S and are illustrated as in Fig. 4(e) and (f) using the 8 × 8 supercell for graphical purposes. In both cases, prominent electron localization is observed around S atoms, attributed to their paired electrons. For DV-2S, there is a repulsion between the two S lone pairs, as evident from the shape of ELF where the red regions point in

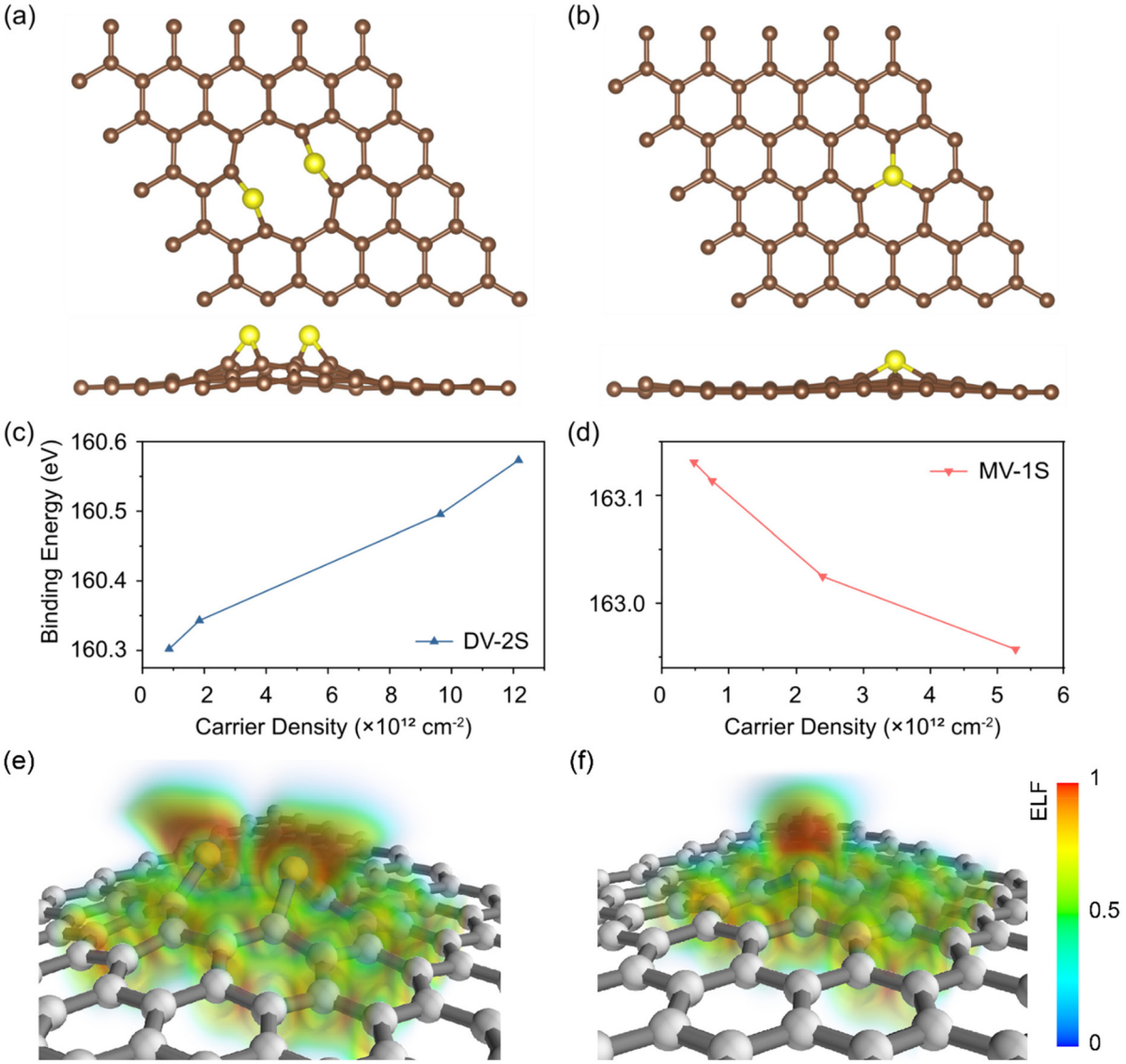

Fig. 4 Top and side views of (a) DV-2S and (b) MV-1S in a 5 × 5 supercell. (c) and (d) Evolution of binding energy with carrier density. (e) and (f) Distribution of ELF around DV-2S and MV-1S. VESTA 20 is used to visualize the atomic structures.[58,59]

opposite directions. In contrast, for MV-1S, the red region for the lone pair points away from the graphene substrate due to the repulsion with the delocalized electrons. Compared to DV-2S, MV-1S exhibits a stronger coupling between C and S atoms, as indicated by its shorter bond length, and higher magnitudes of electron density (ρ) and Laplacian ($\nabla^2\rho$) at bond critical points (BCP). These properties, summarized in Table S1, provide valuable insights into the nature of the C–S bonds. Furthermore, a comparison of the ellipticities reveals that the electron density in the S–C bond is more preferentially accumulated within the graphene plane for MV-1S (ellipticity of 0.120) than for DV-2S (ellipticity of 0.113).[60]

Since an increased etching area is observed in S-doped graphene after vacuum annealing, substitution' is assumed to be the dominant S-doping mechanism, where C atoms in the pristine graphene lattice are replaced by S atoms. Furthermore, both V_1(5–9) and V_2(5–8–5) have been experimentally observed in graphene,[61–65] and so an 'incorporation' mechanism might exist simultaneously, where S atoms are incorporated into existing vacancy defects. The defect formation energies of DV-2S and MV-1S are listed in Table 1 and, in all cases, formation energies increase with defect density leading to a more extended structural deformation across the sheet. For the dominant 'substitution' mechanism, the formation energies of DV-2S are 0.59 to 0.74 eV lower than those of MV-1S, and the difference is more prominent at lower densities, making DV-2S energetically more favorable. Formation energies *via* the 'incorporation' mechanism (E_f^{inc}) show that the incorporation of S atoms stabilizes the defect-laden structure, with only the one exception of DV-2S at the highest density considered. The stabilization of V_2(5–8–5) by S also suggests the interesting possibility that S atoms might accumulate around more

Table 1 Defect densities and formation energies of DV-2S and MV-1S

	Density of S ($\times 10^{13}$ cm^{-2})		E_f^{sub} (eV)		E_f^{inc} [a] (eV)	
Supercell	DV-2S	MV-1S	DV-2S	MV-1S	DV-2S	MV-1S
10 × 10	3.85	1.92	3.30	4.04	−0.48	−4.13
8 × 8	6.03	3.00	3.35	4.12	−0.42	−4.10
5 × 5	15.41	7.64	3.50	4.18	−0.14	−4.03
4 × 4	23.93	11.88	3.62	4.21	0.17	−4.01

[a] For DV-2S, the formation energy of the V_2(5–8–5) divacancy is used as E_{VG}; for MV-1S, the formation energy of the V_1(5–9) monovacancy is used. The nomenclature used in previous research[24,65] is employed for vacancies.

extended defects with similar structures, such as dislocations[66] and linear armchair defects.[67] The value of E_f^{inc} for MV-1S is significantly higher due to the saturation of the under-coordinated C. However, fast transitions from V_1(5–9) towards the more stable V_2(5–8–5) have been observed,[65] indicating that the under-coordinated C might not exist in a stable state under ambient conditions due to its high reactivity.

By comparing the binding energies and formation energies of DV-2S and MV-2S, it can be concluded that, for the S-doped graphene synthesized in this work, C–S–C is the dominant bonding type between S and C. To investigate the electronic properties of S-doped graphene, the electronic structures of DV-2S are analyzed next.

In order to characterize the charge transfer between S and C, the net charge is calculated as the difference between the Mulliken population and the nuclear atomic charge (16 for S and 6 for C) and the results are shown in Fig. 5. The charge transfer per atom is less than 0.1e due to the similar electronegativities of S (2.58) and C (2.55). The averaged charge transfer converges to negligible values beyond the third nearest neighbors of DV-2S, indicating its localized influence on the electronic structure of graphene. Interestingly, the most charge-accumulated and charge-depleted atoms are the nearest and the second-nearest neighbors of DV-2S. The delocalized π band electrons in graphene might contribute to this phenomenon, while the out-of-plane S atoms are limited by the more localized electron states. As the defect density decreases, charge transfer becomes even more localized around the defect, where the charge accumulation at S increases and the oscillation of averaged charge transfer decreases. The observed trend is consistent with the evolution of structural distortions of DV-2S.

The electron band structure and projected density of states (DOS) of DV-2S are shown in Fig. 6. The 6-fold symmetry of graphene's first Brillouin zone (1BZ) is broken due to the DV-2S defect,[68] and so the illustrated path is adopted to sample Dirac point. In all cases, the Fermi level is below the Dirac point, so graphene is p-doped by DV-2S, which is more prominent at higher defect densities, showing good agreement with experimental results. The unique linear dispersion of pristine graphene at the Dirac point is preserved, indicating that the influence of S-doping on carrier mobility might be negligible. The projected DOS shows localized defect levels of approximately −0.36 to −0.67 eV, whose position relative to the Dirac point is almost constant in all cases. Therefore, it can be inferred that p-doping might decrease with defect density, reducing the energies of both the Dirac point and the defect state.

3.4. Protective role of HMDS coating during sulfur annealing

Further investigation into the annealing conditions of graphene was conducted by applying a protective coating on its surface to mitigate damage caused during sulfur annealing. In this study, graphene samples on 90 nm SiO_2 were coated with self-assembled monolayers (SAMs) of HMDS using the immersion method. The choice of HMDS was based on previous

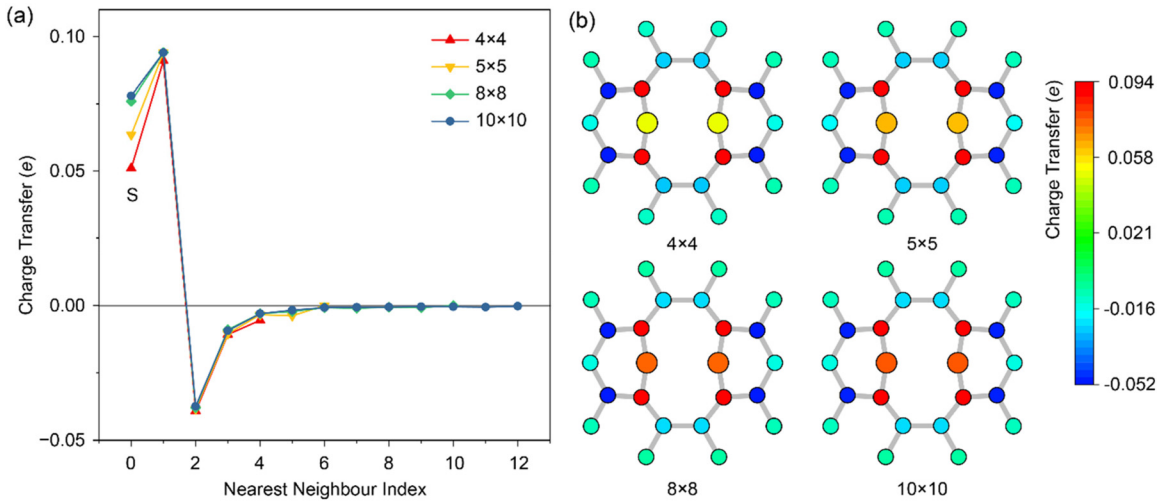

Fig. 5 (a) Charge transfer averaged over the i^{th} nearest neighbor of DV-2S. (b) Distribution of charge transfers up to the third nearest neighbors of DV-2S as a function of the supercell size $n \times n$ (n = 4, 5, 8, 10) of the primitive cell with a lattice parameter of 2.45 Å.

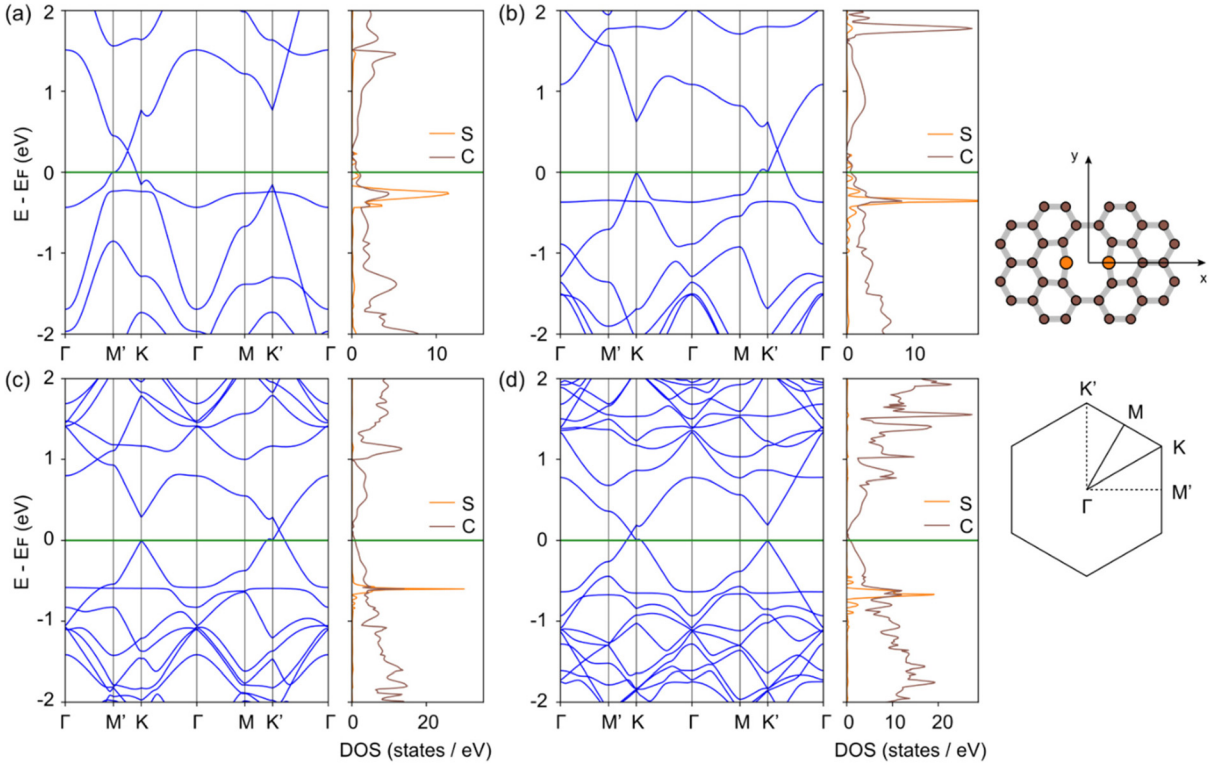

Fig. 6 Electron band structures and projected DOS of DV-2S in (a) 4 × 4, (b) 5 × 5, (c) 8 × 8 and (d) 10 × 10 supercells. E_F is the Fermi energy aligned to 0 eV. The inset shows the highly symmetrical path in the 1BZ and the corresponding directions in real space. CRYSTALpytools[59] is used to visualize the electronic structures.

research which demonstrated that graphene coated with HMDS can withstand high-temperature annealing.[15] HMDS has also been shown to effectively protect graphene during plasma exposure while maintaining its electrical properties intact.[69] The graphene-HMDS samples as shown in Fig. S9 were annealed at 400 °C under sulfur conditions for 10 minutes, followed by vacuum annealing at 800 °C for 15 minutes. In the images, no visible etched pits can be observed on the graphene surface, in contrast to the samples without HMDS coating. Furthermore, the AFM results show that the surface roughness is as low as 0.373 nm. This suggests that the HMDS coating effectively protected the graphene surface from damage during the annealing process.

Subsequently, Raman spectra were acquired for the graphene-HMDS samples under three distinct conditions: before annealing, after the 400 °C sulfur annealing, and then after the 400 °C sulfur annealing followed by the 800 °C vacuum annealing. The analysis focused on the G and 2D peaks, as illustrated in Fig. S9. The observations before annealing indicated only a minor level of doping in the graphene-HMDS sample ($n \sim 4.0 \times 10^{11}$ cm^{-2}) without any noticeable strain. After subjecting the sample to annealing at 400 °C in the presence of sulfur, there was a slight increase in doping ($n \sim 5.7 \times 10^{11}$ cm^{-2}) with minimal strain effects ($\varepsilon \sim +0.37\%$). This outcome is notably different from that found in earlier graphene samples without HMDS coating, which exhibited increased strain ($\varepsilon \sim +0.56\%$) along with higher doping ($n \sim 1.2 \times 10^{12}$ cm^{-2}) after the 400 °C sulfur annealing. However, in the case of the graphene-HMDS sample, only a slight strain effect ($\varepsilon \sim +0.37\%$) was observed when annealed with sulfur at 400 °C followed by further annealing at 800 °C under vacuum. This was accompanied by a marginal reduction in doping with a concentration of $n \sim 5.4 \times 10^{11}$ cm^{-2}. This finding could have been influenced by the reduced presence of sulfur in the graphene-HMDS sample as compared to previous graphene samples, where the S 2p peaks are considerably lower, exhibiting atomic concentrations relative to carbon at approximately 0.29% and 1.15% for samples annealed at 400 °C with sulfur and at 400 °C with sulfur followed by 800 °C in vacuum respectively.

This outcome suggests that the HMDS coating successfully protected the graphene from damage during the annealing process, as indicated by the reduction in strain and doping levels. This protection was particularly evident when annealing was performed in sulfur-rich conditions followed by high-temperature annealing. These results align with our findings that the occurrence of etched pit damage on the graphene surface was significantly reduced with the implementation of HMDS coating.

The presence of sulfur on the graphene surface contributes to an increase in resistance in graphene devices. Furthermore, an increase in annealing temperature under sulfur conditions

leads to higher resistance compared to pristine graphene, as illustrated in Fig. S10(b), where the changes in resistance relative to pre-annealing are estimated to be 190%, 370%, and 160% for samples annealed with sulfur at 300 °C, 400 °C, and 500 °C respectively (Fig. 7). It is noteworthy that samples annealed under sulfur conditions followed by annealing at 800 °C in a vacuum exhibited almost no conductivity, with resistance levels recorded in the GΩ for samples annealed with sulfur at 300 °C, 400 °C, and 500 °C followed by 800 °C in vacuum. However, the samples treated with HMDS showed significantly less increase in resistance compared with the untreated samples. This improvement suggests that the coating with HMDS enables the deposition of TMDCs onto graphene without compromising its quality.

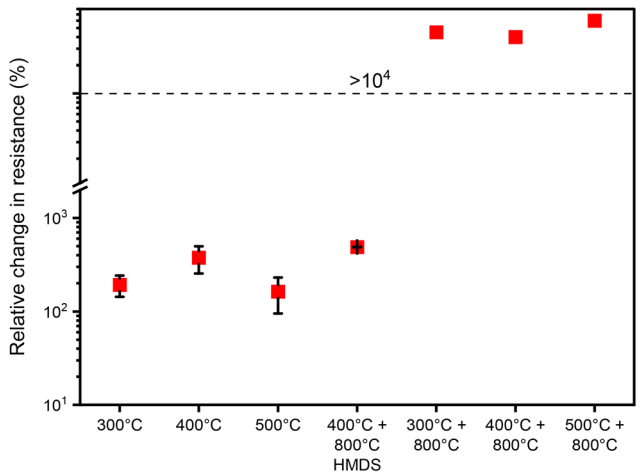

Fig. 7 Influence of sulfur annealing on graphene resistance. A notable increase in resistance is seen with higher annealing temperatures under sulfur conditions. The relative change in resistance compared to pre-annealing is quantified as 190%, 370%, and 160%-for samples annealed with sulfur at 300 °C, 400 °C, and 500 °C respectively. Remarkably, samples subjected to sulfur annealing followed by an 800 °C vacuum annealing exhibit nearly negligible conductivity, with resistance levels reaching GΩ for all samples annealed with sulfur followed by annealing at 800 °C in vacuum. Meanwhile, the application of HMDS leads to a significantly lower increase in resistance compared to uncoated samples.

The performance of HMDS-coated graphene compared to bare graphene under sulfur annealing is summarized in Table 2:

3.5. Implications for TMDC growth on graphene

For HMDS to be integrated into the process of the growth of TMDCs on graphene, it is essential that its presence does not compromise the quality of the TMDC film. Therefore, we deposited a thin film of WS_2 on HMDS-coated graphene using the electrodeposition method. As a precursor, $[NEt_4]_2[WS_2Cl_4]$ was employed as a single-source compound that readily dissolves in CH_2Cl_2 electrolytes.[16,17] Fig. 8(c) presents Raman spectra focusing on the WS_2 region, which has been deconvoluted into several peaks through Lorentzian fitting. The first order $E^1_{2g}(\Gamma)$ mode corresponds to the in-plane lattice vibration[70] and exhibits peaks at 357.2 cm^{-1}. It overlaps slightly with the second order longitudinal acoustic mode (2LA (M)) originating from the coupling of the electronic band structure with lattice vibration,[70] which exhibits peaks at 350.1 cm^{-1}. Meanwhile, the first order $A_{1g}(\Gamma)$ mode signifying out-of-plane lattice displacement[70] is observed at 419.0 cm^{-1}. The shift difference between the $E^1_{2g}(\Gamma)$ and $A_{1g}(\Gamma)$ peaks is measured at 61.8 cm^{-1}. Furthermore, the intensity ratio between the 2LA(M) and A_1g peaks has been calculated to be 1.77. These peak positions and intensity ratios align consistently with the established characteristics of the WS_2 Raman spectra documented in prior studies,[16] which suggests that comparatively high-quality WS_2 has been deposited onto the HMDS-coated graphene. A subsequent XPS analysis (Fig. 8(e) and (f)) focused on the tungsten 4f (W 4f), sulfur 2p (S 2p), and carbon 1s (C 1s) regions. Two distinct doublets were observed in the W 4f region. The first was identified as related to WS_2 formation, exhibiting binding energies of 32.4 eV and 34.5 eV corresponding to W $4f_{5/2}$ and W $4f_{7/2}$ respectively, and the second doublet observed at a higher binding energy (W $4f_{7/2}$ ~ 35.5 eV and W $4f_{5/2}$ ~ 37.8 eV) is associated with oxidation (W^{6+} peaks) and could be linked to surface oxidation leading to WO_3 formation. Meanwhile, the S 2p region with S $2p_{1/2}$ and S $2p_{3/2}$ peaks corresponding to WS_2 formation were recorded at 162.0 eV and 163.2 eV respectively. Again, this suggests that a comparatively high-quality WS_2 has been deposited on the HMDS-coated graphene.

Table 2 Performance comparison of HMDS-protected graphene and bare graphene under Sulfur annealing

Parameter	Bare graphene	HMDS coated graphene
Etched pits	Visible etched pits observed after sulfur annealing and subsequent high-temperature annealing	No visible etched pits observed, even after sulfur annealing at 400 °C and vacuum annealing at 800 °C
Doping level (n)	After 400 °C sulfur annealing: ~1.2×10^{12} cm^{-2} After 800 °C vacuum annealing: ~1.9×10^{12} cm^{-2}	After 400 °C sulfur annealing: ~5.7×10^{11} cm^{-2} After 800 °C vacuum annealing: ~5.4×10^{11} cm^{-2}
Strain (ε)	After 400 °C sulfur annealing: ~+0.56% After 800 °C vacuum annealing: ~+0.54%	After 400 °C sulfur annealing: ~+0.37% After 800 °C vacuum annealing: ~+0.37%
Sulfur content (S 2p peaks)	Atomic concentrations relative to carbon: ~3.53% (400 °C sulfur) and ~1.06% (400 °C sulfur + 800 °C)	Atomic concentrations, significantly reduced sulfur content: ~0.29% (400 °C sulfur) and ~1.15% (400 °C sulfur + 800 °C)
Resistance change (%)	300 °C sulfur: ~190% 400 °C sulfur: ~370% 500 °C sulfur: ~160% 800 °C vacuum: GΩ (negligible conductivity)	400 °C sulfur and 800 °C vacuum: ~480%

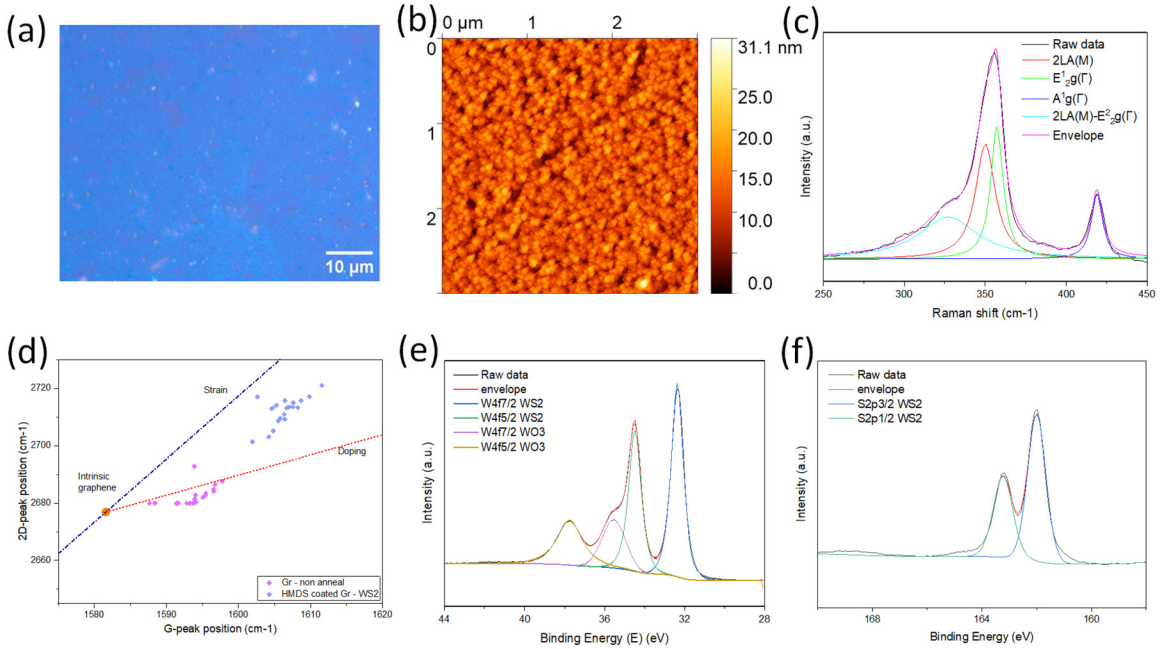

Fig. 8 Multifaceted characterization of WS_2 on HMDS coated graphene. (a) Optical image captured at 100× magnification illustrating successful WS_2 deposition on graphene. (b) AFM image providing insight into the WS_2 morphology on graphene. (c) Raman spectra focusing on the WS_2 region, revealing distinct peaks corresponding to the in-plane lattice vibration ($E^1_{2g}(\Gamma)$), longitudinal acoustic mode (2LA(M)), and out-of-plane lattice displacement ($A^1_g(\Gamma)$). (d) Raman peak analysis of graphene emphasizing G and 2D peaks in correlation analysis of 2D–G peak position with strain and doping. Minor doping is observed with elevated strain. (e) XPS analysis targeting the tungsten 4f (W 4f) region, indicating the presence of WS_2 with characteristic doublets and a second doublet associated with oxidation. (f) XPS analysis focusing on the sulfur 2p (S 2p) region, highlighting peaks corresponding to WS_2 formation. The S 2p1/2 and S 2p3/2 peaks are recorded at 162.0 eV and 163.2 eV, respectively. These comprehensive analyses collectively affirm the successful deposition and characteristics of WS_2 on HMDS-coated graphene.

Evidence of the quality of the electrodeposited WS_2 is further supported by previous STEM studies that compared electrodeposited MoS_2 and WS_2 films grown on graphene electrodes to those grown using chemical vapor deposition (CVD) and other techniques.[16,30] STEM measurements revealed the formation of polycrystalline MoS_2 and WS_2 layers with domain sizes ranging between 10–50 nm.

These findings support the conclusion that high-quality WS_2 film has been deposited on the HMDS-coated graphene. Maintenance of the integrity of graphene after sulfur annealing using HMDS enables the growth of TMDCs using electrodeposition or CVD on graphene, thereby facilitating applications requiring the low resistivity of graphene.

4. Conclusion

This study explores the interaction of sulfur with graphene at different annealing temperatures, its impact on the properties of graphene and its integration with transition metal dichalcogenides. It is demonstrated that the annealing of graphene at high temperatures in the presence of sulfur leads to significant etching, the extent of which increases at higher annealing temperatures. Additionally, substantial post-annealing degradation in the electrical properties of the graphene was observed.

DFT calculations were performed on two hypothetical defects, MV-1S and DV-2S, in order to identify the favourable defect structure in sulfur-doped graphene. Having computed the XPS binding energy and defect formation energy, a DV-2S defect with C–S–C bonds was identified as the most favourable type. This defect induces p-doping in graphene, with doping levels increasing alongside defect density, as also seen in experimental observations. As defect density decreases, both structural distortion and charge transfer become more localized around the sulfur atoms, while the energy between the Dirac point and defect level remains almost constant.

Although defects in sulfur-doped graphene may be more complex than the DV-2S type studied, the strong correlation between theoretical and experimental data suggests that the properties analysed are dominated by the C–S–C bond rather than the specific defect structure. Therefore, the findings of this study not only further our understanding of the structure and electronics of sulfur-doped graphene but also provide a reference for future research on other defects involving the C–S–C bond.

Furthermore, we found that the application of self-assembled monolayers of HMDS on graphene improves its quality and preserves its properties during high-temperature sulfur annealing. This enables the deposition of high-quality TMDCs onto the graphene without compromising its integrity. In essence, this work lays the foundations for the develop-

ments of the controlled growth of TMDC materials on graphene *via* chemical vapour deposition or electrodeposition, thereby unlocking their potential incorporation in high-performance electronic and optoelectronic devices.

Author contributions

Investigation and methodology: Ahmad N. M. M., V. Greenacre, H. Zhou, S. Thomas, G. Mallia, S. Ramadan. Writing of original draft: Ahmad N. M. M., V. Greenacre, H. Zhou, S. Thomas, G. Mallia, S. Ramadan. Software: H. Zhou, G. Mallia, N. Harrison. Project supervision: S. Ramadan, Y. Noori, G. Mallia, N. Harrison, G. Reid, P. Bartlett, K. de Groot, P. Petrov, N. Klein. Writing– review & editing: Ahmad N. M. M., V. Greenacre, H. Zhou, S. Thomas, T. Yin, S. Alodan, Y. Noori, G. Mallia, N. Harrison, G. Reid, P. Bartlett, K. de Groot, S. Ramadan, P. Petrov. Conceptualization: Ahmad N. M. M., S. Ramadan, P. Petrov, N. Klein.

Conflicts of interest

There are no conflicts to declare.

Data availability

The data supporting this article have been included as part of the SI.

The Supplementary Information includes, a description about doping and strain, supplementary figures and tables about characterisation techniques including optical images of graphene morphology at various annealing conditions, estimation of etched area ratios, additional XPS data and extended Raman analysis, defect density strain *etc*. See DOI: **https://doi.org/10.1039/d5nr01917f**.

Acknowledgements

This work was supported by the UK Engineering and Physical Science Research Council (EPSRC) through the joint Grants EP/V062387/1, EP/V062689/1 and EP/V062603/1. Thanks go to Kementerian Pengajian Tinggi Malaysia (Ministry of Higher Education Malaysia) and Universiti Teknikal Malaysia Melaka (UTeM) for PhD sponsorship. H. Z., G. M. and N. H. acknowledge the Research Computing Service at Imperial College London and the ARCHER2 UK national supercomputing service. Access to ARCHER2 was obtained *via* the UKCP consortium funded by EPSRC grant ref EP/X035891/1. The authors deeply appreciate the significant contributions made by Professor Norbert Klein to this research. Tragically, Professor Klein passed away shortly after the completion of this work. This paper is dedicated to his memory and to his enduring legacy in the field of science and engineering.

References

1 S. Ramadan, R. Lobo, Y. Zhang, L. Xu, O. Shaforost, D. K. H. Tsang, J. Feng, T. Yin, M. Qiao, A. Rajeshirke, L. R. Jiao, P. K. Petrov, I. E. Dunlop, M. M. Titirici and N. Klein, *ACS Appl. Mater. Interfaces*, 2021, **13**, 7854–7864.
2 L. Xu, S. Ramadan, B. G. Rosa, Y. Zhang, T. Yin, E. Torres, O. Shaforost, A. Panagiotopoulos, B. Li, G. Kerherve, D. K. Kim, C. Mattevi, L. R. Jiao, P. K. Petrov and N. Klein, *Sens. Diagn.*, 2022, **1**, 719–730.
3 L. Liao and X. Duan, *Mater. Today*, 2012, **15**(7–8), 328–338.
4 J. Wang, X. Mu, M. Sun and T. Mu, *Appl. Mater. Today*, 2019, **16**, 1–20.
5 T. Yin, L. Xu, B. Gil, N. Merali, M. S. Sokolikova, D. C. A. Gaboriau, D. S. K. Liu, A. N. Muhammad Mustafa, S. Alodan, M. Chen, O. Txoperena, M. Arrastua, J. M. Gomez, N. Ontoso, M. Elicegui, E. Torres, D. Li, C. Mattevi, A. E. Frampton, L. R. Jiao, S. Ramadan and N. Klein, *ACS Nano*, 2023, **17**(15), 14619–14631.
6 S. K. Chakraborty, B. Kundu, B. Nayak, S. P. Dash and P. K. Sahoo, *iScience*, 2022, **25**(3), 103942.
7 M. Wu, Y. Xiao, Y. Zeng, Y. Zhou, X. Zeng, L. Zhang and W. Liao, *InfoMat*, 2021, **3**, 362–396.
8 B. Huet, S. Bachu, N. Alem, D. W. Snyder and J. M. Redwing, *Carbon*, 2023, **202**, 150–160.
9 S. Mitra, S. Kakkar, T. Ahmed and A. Ghosh, *Phys. Rev. Appl.*, 2020, **14**, 064029.
10 A. Yadav, S. Kumar, A. Kumar and P. Sharan, *Front. Mater.*, 2022, **9**, 1106251.
11 T. Iqbal, S. Fatima, T. Bibi and M. Zafar, *Opt. Quant. Electron.*, 2021, **53**, 228.
12 Q. Lv and R. Lv, *Carbon*, 2019, **145**, 240–250.
13 G. Piccinini, S. Forti, L. Martini, S. Pezzini, V. Miseikis, U. Starke, F. Fabbri and C. Coletti, *2D Mater.*, 2020, **7**, 014002.
14 T. Kaplas, V. Jakstas, A. Biciunas, A. Luksa, A. Setkus, G. Niaura and I. Kasalynas, *Condens. Matter*, 2019, **4**, 21.
15 Y. Wang, A. Guerenneur, S. Ramadan, J. Huang, S. Fearn, N. Nabi, N. Klein, N. McN. Alford and P. K. Petrov, *ACS Appl. Electron. Mater.*, 2023, **5**, 3261–3267.
16 Y. J. Noori, S. Thomas, S. Ramadan, V. K. Greenacre, N. M. Abdelazim, Y. Han, J. Zhang, R. Beanland, A. L. Hector, N. Klein, G. Reid, P. N. Bartlett and C. H. de Groot, *2D Mater.*, 2021, **9**, 15025.
17 S. Thomas, V. K. Greenacre, D. E. Smith, Y. J. Noori, N. M. Abdelazim, A. L. Hector, C. H. (Kees) de Groot, W. Levason, P. N. Bartlett and G. Reid, *Chem. Commun.*, 2021, **57**, 10194–10197.
18 R. Dovesi, A. Erba, R. Orlando, C. M. Zicovich-Wilson, B. Civalleri, L. Maschio, M. Rérat, S. Casassa, J. Baima, S. Salustro and B. Kirtman, *Wiley Interdiscip. Rev.: Comput. Mol. Sci.*, 2018, **8**, e1360.
19 R. Dovesi, F. Pascale, B. Civalleri, K. Doll, N. M. Harrison, I. Bush, P. D'Arco, Y. Noel, M. Rera, P. Carbonniere, M. Causa, S. Salustro, V. Lacivita, B. Kirtman, A. M. Ferrari, F. S. Gentile, J. Baima, M. Ferrero, R. Demichelis and M. De La Pierre, *J. Chem. Phys.*, 2020, **152**, 204111.

20 A. Erba, J. K. Desmarais, S. Casassa, B. Civalleri, L. Donà, I. J. Bush, B. Searle, L. Maschio, L. Edith-Daga, A. Cossard, C. Ribaldone, E. Ascrizzi, N. L. Marana, J. P. Flament and B. Kirtman, *J. Chem. Theory Comput.*, 2023, **19**(20), 6891–6932.
21 J. Heyd, G. E. Scuseria and M. Ernzerhof, *J. Chem. Phys.*, 2003, **118**, 8207–8215.
22 L. Pisani, B. Montanari and N. M. Harrison, *New J. Phys.*, 2008, **10**, 033002.
23 L. Pisani, J. A. Chan, B. Montanari and N. M. Harrison, *Phys. Rev. B: Condens. Matter Mater. Phys.*, 2007, **75**, 064418.
24 H. Zhou, G. Mallia and N. M. Harrison, *J. Phys. Chem. C*, 2022, **126**(45), 19435–19445.
25 F. Savazzi, F. Risplendi, G. Mallia, N. M. Harrison and G. Cicero, *J. Phys. Chem. Lett.*, 2018, **9**(7), 1746–1749.
26 C. Adamo, V. Barone, A. Bencini, R. Broer, M. Filatov, N. M. Harrison, F. Illas, J. P. Malrieu and I. D. P. R. Moreira, *J. Chem. Phys.*, 2006, **124**, 107101.
27 M. Catti, A. Pavese, R. Dovesi and V. R. Saunders, *Phys. Rev. B: Condens. Matter Mater. Phys.*, 1993, **47**, 9189.
28 M. M. Francl, W. J. Pietro, W. J. Hehre, J. S. Binkley, M. S. Gordon, D. J. DeFrees and J. A. Pople, *J. Chem. Phys.*, 1982, **77**, 3654–3665.
29 D. Gray, A. Mccaughan and B. Mookerji, *Physics for Solid State Applications*, 2009, vol. 2.
30 Y. J. Noori, S. Thomas, S. Ramadan, D. E. Smith, V. K. Greenacre, N. Abdelazim, Y. Han, R. Beanland, A. L. Hector, N. Klein, G. Reid, P. N. Bartlett and C. H. Kees De Groot, *ACS Appl. Mater. Interfaces*, 2020, **12**(44), 49786–49794.
31 Z. Zhu, S. Zhan, J. Zhang, G. Jiang, M. Yi and J. Wen, *Mater. Res. Express*, 2019, **6**, 095011.
32 J. Han, R. Fang, L. Zhu, Z. Geng and X. He, *Ferroelectrics*, 2020, **562**(1), 51.
33 Y. Gu, M. Zheng, Y. Liu and Z. Xu, *J. Am. Ceram. Soc.*, 2007, **90**(5), 1589–1591.
34 I. Vlassiouk, M. Regmi, P. Fulvio, S. Dai, P. Datskos, G. Eres and S. Smirnov, *ACS Nano*, 2011, **5**(7), 6069–6076.
35 C. Bautista-Flores, J. S. Arellano-Peraza, R. Y. Sato-Berrú, E. Camps and D. Mendoza, *Chem. Phys. Lett.*, 2016, **665**, 121–126.
36 S. Alotibi, T. F. Qahtan, A. M. Alansi, T. O. Owolabi, S. T. Hameed, N. Afzal, S. Bilal and D. Salah, *Coatings*, 2024, **14**(5), 534.
37 W. Liu and G. Speranza, *ACS Omega*, 2021, **6**(9), 6195–6205.
38 B. Gupta, N. Kumar, K. Panda, V. Kanan, S. Joshi and I. Visoly-Fisher, *Sci. Rep.*, 2017, **7**, 45030.
39 O. Odunmbaku, J. Song, S. Wang, A. Taallah, Y. Dai, W. Li, W. Li, Y. He, J. Guo, H. Zhang and F. S. Boi, *Carbon Trends*, 2021, **5**, 100102.
40 S. Berciaud, S. Ryu, L. E. Brus and T. F. Heinz, *Nano Lett.*, 2009, **9**, 346–352.
41 J. E. Lee, G. Ahn, J. Shim, Y. S. Lee and S. Ryu, *Nat. Commun.*, 2012, **3**, 1024.
42 A. Das, S. Pisana, B. Chakraborty, S. Piscanec, S. K. Saha, U. V. Waghmare, K. S. Novoselov, H. R. Krishnamurthy, A. K. Geim, A. C. Ferrari and A. K. Sood, *Nat. Nanotechnol.*, 2008, **3**, 210–215.
43 A. Das, B. Chakraborty, S. Piscanec, S. Pisana, A. K. Sood and A. C. Ferrari, *Phys. Rev. B: Condens. Matter Mater. Phys.*, 2009, **79**, 155417.
44 F. Ding, H. Ji, Y. Chen, A. Herklotz, K. Dörr, Y. Mei, A. Rastelli and O. G. Schmidt, *Nano Lett.*, 2010, **10**(9), 3453–3458.
45 C. Metzger, S. Rémi, M. Liu, S. V. Kusminskiy, A. H. Castro Neto, A. K. Swan and B. B. Goldberg, *Nano Lett.*, 2010, **10**(1), 6–10.
46 M. Bruna, A. K. Ott, M. Ijäs, D. Yoon, U. Sassi and A. C. Ferrari, *ACS Nano*, 2014, **8**(7), 7432–7441.
47 T. M. G. Mohiuddin, A. Lombardo, R. R. Nair, A. Bonetti, G. Savini, R. Jalil, N. Bonini, D. M. Basko, C. Galiotis, N. Marzari, K. S. Novoselov, A. K. Geim and A. C. Ferrari, *Phys. Rev. B: Condens. Matter Mater. Phys.*, 2009, **79**, 205433.
48 M. Mohr, J. Maultzsch and C. Thomsen, *Phys. Rev. B: Condens. Matter Mater. Phys.*, 2010, **82**, 201409(R).
49 S. Pisana, M. Lazzeri, C. Casiraghi, K. S. Novoselov, A. K. Geim, A. C. Ferrari and F. Mauri, *Nat. Mater.*, 2007, **6**, 198–201.
50 M. Lazzeri and F. Mauri, *Phys. Rev. Lett.*, 2006, **97**, 266407.
51 S. Ryu, L. Liu, S. Berciaud, Y. J. Yu, H. Liu, P. Kim, G. W. Flynn and L. E. Brus, *Nano Lett.*, 2010, **10**(12), 4944–4951.
52 M. Ishigami, J. H. Chen, W. G. Cullen, M. S. Fuhrer and E. D. Williams, *Nano Lett.*, 2007, **7**, 1643–1648.
53 N. S. Mueller, S. Heeg, M. P. Alvarez, P. Kusch, S. Wasserroth, N. Clark, F. Schedin, J. Parthenios, K. Papagelis, C. Galiotis, M. Kalbáč, A. Vijayaraghavan, U. Huebner, R. Gorbachev, O. Frank and S. Reich, *2D Mater.*, 2018, **5**, 015016.
54 P. A. Denis, R. Faccio and A. W. Mombru, *ChemPhysChem*, 2009, **10**(4), 715–722.
55 J. Tuček, P. Błoński, Z. Sofer, P. Šimek, M. Petr, M. Pumera, M. Otyepka and R. Zbořil, *Adv. Mater.*, 2016, **28**(25), 5045–5053.
56 S. Tardio and P. J. Cumpson, *Surf. Interface Anal.*, 2018, **50**(1), 5–12.
57 Z. Yang, Z. Yao, G. Li, G. Fang, H. Nie, Z. Liu, X. Zhou, X. Chen and S. Huang, *ACS Nano*, 2012, **6**(1), 205–211.
58 K. Momma and F. Izumi, *J. Appl. Crystallogr.*, 2011, **44**(6), 1272–1276.
59 B. Camino, H. Zhou, E. Ascrizzi, A. Boccuni, F. Bodo, A. Cossard, D. Mitoli, A. M. Ferrari, A. Erba and N. M. Harrison, *Comput. Phys. Commun.*, 2023, **292**, 108853.
60 R. F. W. Bader, *Chem. Rev.*, 1991, **91**(5), 893–928.
61 A. W. Robertson, B. Montanari, K. He, J. Kim, C. S. Allen, Y. A. Wu, J. Olivier, J. Neethling, N. Harrison, A. I. Kirkland and J. H. Warner, *Nano Lett.*, 2013, **13**(4), 1468–1475.
62 A. W. Robertson, B. Montanari, K. He, C. S. Allen, Y. A. Wu, N. M. Harrison, A. I. Kirkland and J. H. Warner, *ACS Nano*, 2013, **7**(5), 4495–4502.
63 J. H. Warner, M. H. Rümmeli, L. Ge, T. Gemming, B. Montanari, N. M. Harrison, B. Büchner and G. A. D. Briggs, *Nat. Nanotechnol.*, 2009, **4**, 500–504.

64 M. M. Ugeda, D. Fernández-Torre, I. Brihuega, P. Pou, A. J. Martínez-Galera, R. Pérez and J. M. Gómez-Rodríguez, *Phys. Rev. Lett.*, 2011, **107**, 116803.
65 J. Kotakoski, A. V. Krasheninnikov, U. Kaiser and J. C. Meyer, *Phys. Rev. Lett.*, 2011, **106**, 105505.
66 F. Banhart, J. Kotakoski and A. V. Krasheninnikov, *ACS Nano*, 2011, **5**(1), 26–41.
67 J. H. Warner, G. Do Lee, K. He, A. W. Robertson, E. Yoon and A. I. Kirkland, *ACS Nano*, 2013, **7**(11), 9860–9866.
68 S. G. Mayo, F. Yndurain and J. M. Soler, *J. Phys.: Condens. Matter*, 2020, **32**, 205902.
69 S. Ramadan, Y. Zhang, D. K. H. Tsang, O. Shaforost, L. Xu, R. Bower, I. E. Dunlop, P. K. Petrov and N. Klein, *ACS Omega*, 2021, **6**, 4767–4775.
70 A. Berkdemir, H. R. Gutiérrez, A. R. Botello-Méndez, N. Perea-López, A. L. Elías, C. I. Chia, B. Wang, V. H. Crespi, F. López-Urías, J. C. Charlier, H. Terrones and M. Terrones, *Sci. Rep.*, 2013, **3**, 1755.